Editors' Suggestion

Depth-resolved amorphization and nonuniformity in square-planar nickelate films

Purnima P. Balakrishnan,[1,*] Maria Bambrick-Santoyo,[2,3] Lin Er Chow,[4] Dan Ferenc Segedin,[2] Mythili Surendran,[5,6] Ranjan K. Patel,[7] Paige E. Quarterman,[1] Shin Muramoto,[8] Grace A. Pan,[2] Zhaoyang Luo,[4] Michael R. Fitzsimmons,[9,10,11] Amanda Huon,[9] Timothy R. Charlton,[9] Christy J. Kinane,[12] Andrew J. Caruana,[12] Hui Wu,[1] Charles M. Brooks,[2] Qi Song,[2] Hanjong Paik,[13] Srimanta Middey,[7] Jayakanth Ravichandran,[14,5,6] A. Ariando,[4] Julia A. Mundy,[2,15] and Alexander J. Grutter[1,†]

[1]*NIST Center for Neutron Research, National Institute of Standards and Technology, Gaithersburg, Maryland 20899, USA*
[2]*Department of Physics, Harvard University, Cambridge, Massachusetts 02138, USA*
[3]*Department of Electrical Engineering and Computer Science, Massachusetts Institute of Technology, Cambridge, Massachusetts 02139, USA*
[4]*Department of Physics, Faculty of Science, National University of Singapore, Singapore 117551, Singapore*
[5]*Mork Family Department of Chemical Engineering and Materials Science, University of Southern California, Los Angeles, California 90089, USA*
[6]*Core Center for Excellence in Nano Imaging, University of Southern California, Los Angeles, California 90089, USA*
[7]*Department of Physics, Indian Institute of Science, Bengaluru 560012, India*
[8]*Material Measurement Laboratory, National Institute of Standards and Technology, Gaithersburg, Maryland 20899, USA*
[9]*Neutron Scattering Division, Oak Ridge National Laboratory, Oak Ridge, Tennessee 37831, USA*
[10]*Department of Physics and Astronomy, University of Tennessee, Knoxville, Tennessee 37996, USA*
[11]*Shull Wollan Center — A Joint Center for Neutron Sciences, Oak Ridge, Tennessee 37831, USA*
[12]*ISIS, Rutherford Appleton Laboratory, Harwell Science and Innovation Campus, Science and Technology Facilities Council, Oxon OX11 0QX, United Kingdom*
[13]*School of Electrical & Computer Engineering, University of Oklahoma, Norman, Oklahoma 73019, USA*
[14]*Ming Hsieh Department of Electrical and Computer Engineering, University of Southern California, Los Angeles, California 90089, USA*
[15]*School of Engineering and Applied Science, Harvard University, Cambridge, Massachusetts 02138, USA*

(Received 15 December 2025; accepted 24 February 2026; published 31 March 2026)

Superconducting nickelate thin films with the layered square-planar structure are synthesized via the topotactic reduction of a more oxygen rich perovskite or Ruddlesden-Popper (RP) phase due to the instability of the target $Ni^{1+\delta}$ valence. The topotactic reduction induces a dramatic structural transformation, which yields high defect densities in the resulting film and has introduced uncertainty regarding film uniformity, particularly as it relates to the calculation of physical parameters based on estimates of superconducting volume fraction. Here we use neutron reflectometry (NR) and secondary ion mass spectrometry (SIMS) to obtain a sub-nm resolved understanding of the structural depth profile across a wide range of layered square-planar nickelates. While the as-grown parent compounds are bulklike and of very high quality, the depth profiles of reduced films are generally nonuniform and indicative of partial amorphization. We identify careful selection of substrate and reduction conditions as promising directions toward mitigating amorphization and improving uniformity.

DOI: 10.1103/9ldc-sk6x

I. INTRODUCTION

Nickel oxides have long been considered an ideal platform for replicating the physics of high critical-temperature (T_c) superconducting cuprates, with the promise of providing a new window into high-temperature superconductivity [1,2]. After years of effort, nickelate superconductivity was finally demonstrated in infinite-layer (Nd,Sr)NiO_2 films in 2019 [3]. Nickelate superconductivity has since been generalized to many other square-planar nickelate compounds, and remains a source of myriad interesting physical phenomena [4–13]. In (Sm,Eu,Ca,Sr)NiO_2, the ambient-pressure T_c for superconductivity reaches 40 K, placing square-planar nickelates firmly in the high-T_c regime [14]. High-T_c superconductivity has also been observed in bulk crystals of RP nickelates such as $La_3Ni_2O_7$, $La_2PrNi_2O_7$, and $La_4Ni_3O_{10}$ under high pressure, and at ambient pressure in strained thin films [15–19]. Although thin films remain the only viable route to ambient-pressure nickelate superconductivity, most superconducting thin film nickelates to date require some postsynthesis chemical treatment to reach zero resistance, introducing fabrication challenges associated with control of the Ni valence through oxygen stoichiometry [18,20–24]. Square-planar nickelate films are obtained by reducing an oxygen-rich parent compound, exploiting the broken symmetry introduced by substrate strain to preferentially remove the apical oxygens, leaving two-dimensional NiO_2 sheets with a nickel d^9 electron configuration [3].

In the square-planar nickelates, challenges in controlling the dramatic structural and electronic change induced by the reduction process often yield multiphase systems with high defect densities, complicating estimates of parameters

*Contact author: purnima.balakrishnan@nist.gov
†Contact author: alexander.grutter@nist.gov

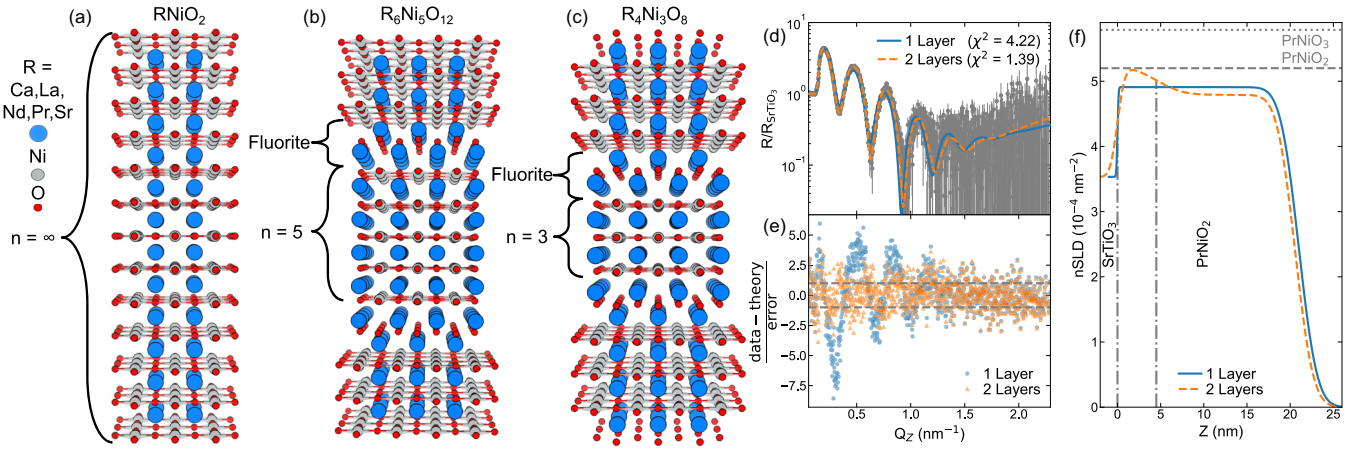

FIG. 1. (a)–(c) Schematic of the (a) $n = \infty$, (b) $n = 5$, and (c) $n = 3$ square-planar structures. (d) Neutron reflectivity, normalized by the theoretical reflectivity of the bare $SrTiO_3$ substrate, from a $PrNiO_2$ film reduced for 3 h at 300 °C. Fits to the data (gray circles) are shown using models assuming either one (solid blue line) or two (dashed orange line) layers to represent the film. (e) Residuals for the fits with using one (blue circles) or two (orange triangles) film layers. (f) Best-fit nSLD profiles for both models, with gray horizontal lines representing ideal theoretical nSLD values of the parent $PrNiO_3$ and reduced $PrNiO_2$, respectively. Gray vertical lines represent interface positions. The substrate surface is defined as Z = 0 nm.

such as critical current densities (J_c) [22,25–27]. Estimates of these values typically average over an entire film, assuming homogeneity [3,4,19]. As such, it is unclear whether the current estimates of bulk values like J_c are representative of the fundamental physics of square-planar nickelates or are artificially low due to inhomogeneity introduced in the topotactic reduction [28,29]. Similarly, confinement effects are known to suppress T_c in many superconductors [30,31]. Accurate comparison of square-planar nickelates with other superconductors therefore requires precise understanding of their spatial uniformity.

There are several proposals as to how the reduction process impacts uniformity. It has been suggested that tensile strain in the parent compound introduces extended defects while compressive strain in the reduced phase can induce *c*-axis reorientation [5,12,21,32]. A polar discontinuity at the substrate/film interface can result in intermixing and altered crystal quality [33,34]. Other studies have shown the presence of surface reconstructions and highlighted the important role of capping layers in stabilizing the film surface and improving overall quality [22,23,35–38]. The impact of the reducing agent has also been much debated, with evidence of high hydrogen concentrations in some films reduced by CaH_2 [39]. It has been suggested that intercalated hydrogen may play a critical role in stabilizing superconductivity, although this has been ruled out by explicit measurements of the hydrogen content and the use of hydrogen-free reduction methods [7,39–45].

Despite these proposals, detailed investigations into the impact of reduction conditions on film uniformity remain challenging. Traditional x-ray reflectometry techniques, which are ideal for probing layered structures, have limited sensitivity to oxygen and hydrogen, which are the elements most active throughout the reduction process. Here, we utilize neutron reflectometry (NR), where the relatively strong interactions with oxygen and hydrogen greatly improve sensitivity to the distribution of these elements along the film growth axis. The NR data are supplemented with x-ray reflectometry (XRR) and secondary ion mass spectrometry (SIMS) measurements to provide a more complete picture of elemental density and chemical distribution.

This work has revealed that only precisely optimized reduction conditions yield vertically uniform films, with 10 °C changes in reduction temperature making the difference between a multilayer sample and a uniform reduction. Optimal reduction conditions and film uniformity vary across nickelate material systems and appear to be at least partially controlled by choice of substrate. Even in the most uniform reduced films, we observe suppression of the nuclear scattering length density (nSLD), suggesting the formation of low-density amorphous regions which are challenging to quantify through x-ray diffraction (XRD) and electron microscopy. We reduce films with isotopically-enriched calcium deuteride (CaD_2) to confirm that the observed nSLD suppression is not due to reduction-induced hydrogen incorporation. The resulting signal from incorporated deuterium (D) is an order of magnitude lower than that of hydrogen. Further, the D content is reduced near the substrate/film interface, suggesting the presence of a chemically distinct region.

II. EXPERIMENTAL DESIGN

Given the range of reported fabrication outcomes, we probe over 30 samples grown by three different research groups, comparing nickelate films of varying quality fabricated via different methods—either molecular beam epitaxy (MBE) or pulsed laser deposition (PLD)—all reduced using CaH_2 or CaD_2. As reduction energetics may vary depending on stoichiometry and structure, we compared multiple square-planar nickelate systems, including $PrNiO_2$, $NdNiO_2$, $Nd_{1-x}Sr_xNiO_2$, $La_{1-x}Ca_xNiO_2$, $Nd_4Ni_3O_8$, and $Nd_6Ni_5O_{12}$. All of these materials are square-planar nickelates with $n = \infty$, 5, or 3, where n represents the number of quasi-2D NiO_2 sheets confined between AO_2 spacer layers, where A is the A-site cation. The structures are illustrated in Figs. 1(a)–1(c).

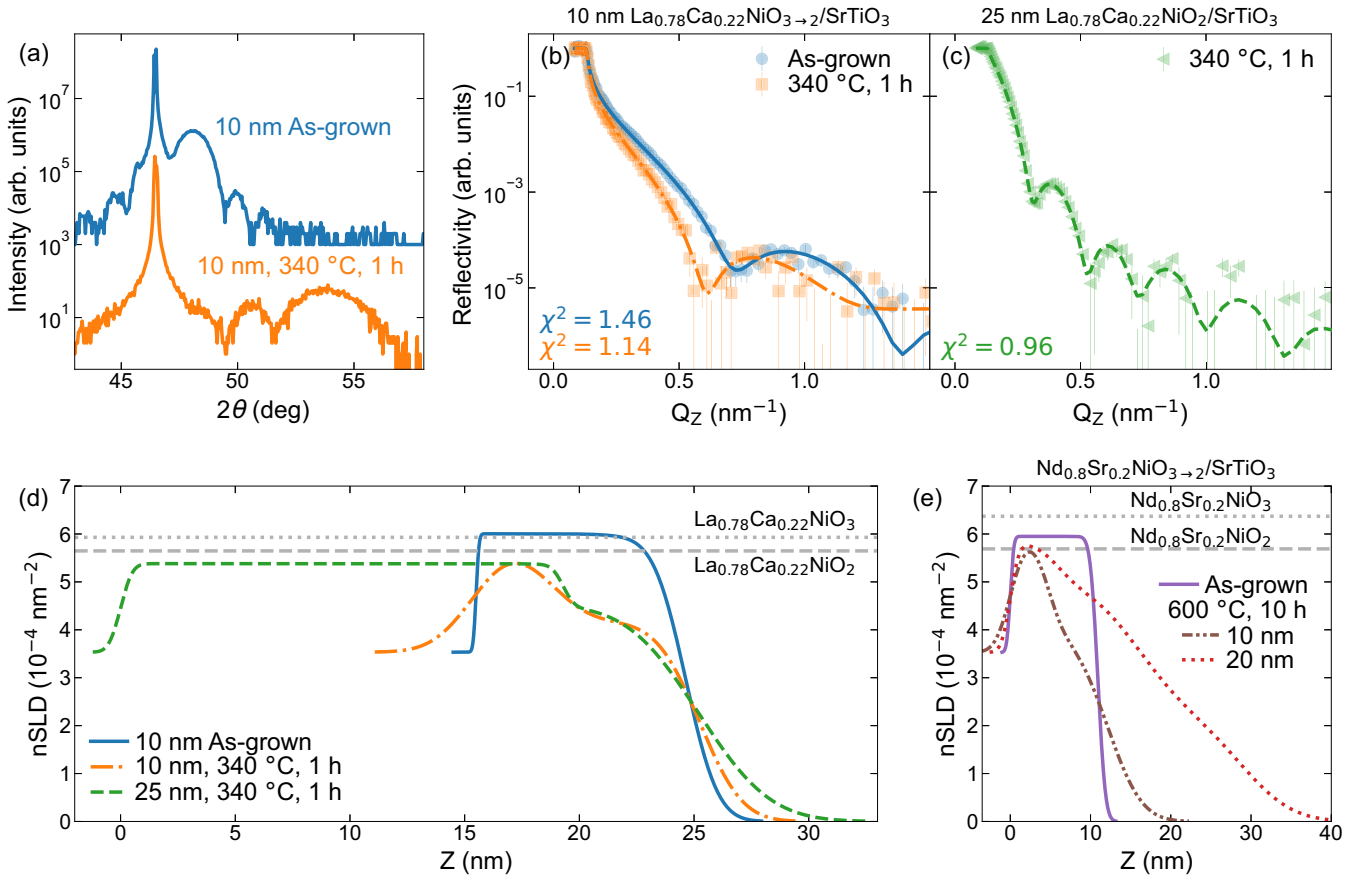

FIG. 2. (a) XRD measurements of 10 nm thick $La_{0.78}Ca_{0.22}NiO_{3\rightarrow2}$, with curves offset for clarity. (b) Neutron reflectivity and fits for 10 nm $La_{0.78}Ca_{0.22}NiO_3$, 10 nm $La_{0.78}Ca_{0.22}NiO_2$, and (c) 25 nm $La_{0.78}Ca_{0.22}NiO_2$. (d) Best-fit nSLD profiles associated with the theory curves in (b) and (c). Curves shifted to align the top interface of all nickelate films for better comparison of the surface layer reconstruction. (e) Best-fit nSLD profiles for 10 nm $Nd_{0.8}Sr_{0.2}NiO_3$, 10 nm $Nd_{0.8}Sr_{0.2}NiO_2$, and 20 nm $Nd_{0.8}Sr_{0.2}NiO_2$ films after CaH_2 reduction at 600 °C for 10 h. Data and fits for the profiles in (e) are shown in the Supplemental Material [47]. Horizontal dotted (dashed) lines represent the ideal expected nSLD values of the as-grown (reduced) films.

Within these spacers, the rare-earth oxide exhibits a fluorite structure. Infinite-layer ($n = \infty$) films have no fluorite layers.

Neutron reflectometry experiments were performed using the PBR and CANDOR instruments at the NIST Center for Neutron Research, the MAGREF instrument at the Spallation Neutron Source, and the Polref instrument at the ISIS Neutron and Muon Source. Instrumental details and measurement conditions can be found in the methods section. For all experiments, we measured the reflected neutron intensity as a function of momentum transfer along the film normal direction (Q_Z). These data were fit to yield the nSLD depth profile, determined by the composition and density of the constituent layers. In cases where the nSLD contrast between the reduced film and the substrate was weak, the data were corefined as needed with an additional XRR measurement using a model with coupled thickness parameters to constrain the fit.

To illustrate the sensitivity of NR to nonuniformity in reduced nickelate films, we examine a typical measurement of a 22 nm thick $PrNiO_2$ film grown on a $SrTiO_3$ substrate and reduced from $PrNiO_3$ via a 3 h, 300 °C anneal in the presence of CaH_2. Figure 1(d) shows the neutron reflectivity normalized by the expected reflectivity of a bare $SrTiO_3$ substrate. The solid blue line is a theoretical fit to the data using a model which assumes a uniform layer of $PrNiO_2$. The dashed orange line is a fit using a model with nonuniform $PrNiO_2$, represented as two "slabs" with different nSLDs in the model. Adding a second layer improves the reduced χ^2 goodness-of-fit parameter from 4.22 to 1.39. The fitting improvement is highlighted in Fig. 1(e), which plots the residuals for both models. The single-layer model exhibits larger residuals with an oscillatory structure, while the two-layer model exhibits reduced residuals with suppressed oscillatory structure. In general, we fit the NR data with the fewest layers required to achieve a high-quality fit. The resulting nSLD profiles for both models are shown in Fig. 1(f), revealing an interfacial layer with increased nSLD and an approximate thickness of 4.5 nm ± 0.3 nm. All quoted uncertainties for NR fitting parameters, such as layer thicknesses, are determined through Bayesian methods as implemented in the DREAM algorithm of the BUMPS Python package [46].

III. REDUCTION TEMPERATURE AND SURFACE RECONSTRUCTIONS

We first consider the effect of potential surface reconstructions in infinite-layer ($n = \infty$) films. A 10 nm thick

$La_{0.78}Ca_{0.22}NiO_3$ film is reduced at 340 °C for 1 h, the typical treatment yielding superconducting $La_{0.78}Ca_{0.22}NiO_2$ [6]. Growth-axis XRD scans of as-grown and reduced $La_{0.78}Ca_{0.22}NiO_{3\rightarrow 2}$ are shown in Fig. 2(a). An as-grown 10 nm $La_{0.78}Ca_{0.22}NiO_3$ film exhibits a strong (002) reflection, while this peak shifts to higher angle in the reduced film, broadening and decreasing in intensity. These observations indicate a successful transformation to the superconducting infinite-layer phase, but also suggest increased defect density or the formation of amorphous regions.

Neutron reflectometry measurements provide depth-resolved insight. The data are shown in Figs. 2(b) and 2(c) alongside theoretical fits, and the resulting nSLD profiles are shown in Fig. 2(d). The as-grown $La_{0.78}Ca_{0.22}NiO_3$ (blue) matches the expected nSLD value and is well fit by a single uniform layer. In contrast, the reduced $La_{0.78}Ca_{0.22}NiO_2$ (dashed orange) contains a surface layer with nSLD suppressed to 73%–80% of the theoretical value and a layer near the substrate/film interface with milder nSLD suppression to 96% of the theoretical value. To understand whether this suppression is a surface effect, we also reduced a thicker 25 nm film, with the corresponding NR data shown in Fig. 2(c). Both 10 nm and 25 nm reduced films have nearly identical 6–7 nm thick surface layers with suppressed nSLD and a higher density region deeper into the film. This result points to potential amorphization at the film surface due to the high reduction temperature.

As a limiting case, we tested a 10 h, 600 °C reduction on $Nd_{0.8}Sr_{0.2}NiO_{3\rightarrow 2}$ films with thicknesses of approximately 10 nm and 20 nm. Data and associated fits are shown in the Supplemental Material, and the extracted nSLD profiles appear in Fig. 2(e) [47–50]. Both samples exhibit a 5–6 nm thick region near the substrate/film interface with nSLD matching the expected value for $Nd_{0.8}Sr_{0.2}NiO_2$, with the rest of the film thicknesses exhibiting dramatically suppressed nSLD. While this study primarily focuses on the reduction of uncapped films, a $Nd_{0.8}Sr_{0.2}NiO_2$ film capped with $SrTiO_3$ was subjected to the same reduction process (10 h at 600 °C). The associated PNR data, fits, and nSLD profiles are shown in the Supplemental Material (Fig. S10) [47]. This sample retains a 3 nm thick region at the substrate/film interface with bulklike nSLD. Previously reported electron microscopy of this sample showed a very thin, highly crystalline layer at the substrate/film interface with highly defective regions above [42].

These data indicate that the reduction process may impose substantial surface reconstructions at the film surface, propagating down into the film with increasing temperature and time. At the same time, substrate templating stabilizes and preserves higher-quality crystal structures near the interface. A key consideration, therefore, is whether reduction condition optimization may enable vertically uniform films to be obtained.

IV. OPTIMIZING DEPTH UNIFORMITY

To address this question, we consider a series of samples cleaved from a single 20 nm $NdNiO_3$ film (growth A) grown by MBE on $SrTiO_3$ substrates and reduced separately. Using portions of a single parent film minimizes sample-to-sample variation in defects, substrate quality, or stoichiometry. Films were reduced by thermal anneal in the presence of CaH_2 powder for varying times (3–6 h) and temperatures (280–300 °C). The full thermal/temporal phase space is shown in Fig. 3(a). XRD measurements in Fig. 3(b), show the evolution of film lattice structure with reduction. The as-grown film has strong (00l) $NdNiO_3$ peaks and well-defined Laue oscillations. The 280 °C, 3 h reduction (blue) exhibits a broad reflection at an intermediate angle between $NdNiO_3$ and $NdNiO_2$. This sample exhibits insulating behavior in electrical transport measurements, shown in Fig. 3(c), suggesting incomplete reduction. Increasing the reduction temperature eliminates the intermediate diffraction peak coincident with the emergence of a broad $NdNiO_2$ peak at higher scattering angle. Reduced films exhibit shifted and broadened film peaks, as expected for a system in which oxygen removal yields a disordered contraction of the c-axis lattice parameter. While all three samples reduced at or above 290 °C appear similar in XRD and are metallic, their electrical resistances differ by more than an order of magnitude. We consider the sample reduced for 6 h at 290 °C optimal, as it exhibits the lowest resistance in the series.

The NR data and associated theoretical fits from all four samples are shown in Fig. 3(d), while the associated nSLD profiles are shown in Figs. 3(e) and 3(f). The nSLD of the under-reduced 280 °C sample resembles the $PrNiO_2$ profile of Fig. 1(c), with a thin (approximately 3.3 nm) layer near the substrate/film interface matching the expected nSLD for $NdNiO_2$ and a thicker layer with suppressed nSLD comprising the bulk of the film. Increasing the reduction temperature to 290 °C yields a less uniform nSLD profile which requires three distinct layers to properly describe, with a higher-nSLD region near the substrate/film interface and a surface region with further suppressed nSLD. The nSLD of all layers is now suppressed below bulk $NdNiO_2$.

Increasing either the anneal time (290 °C, 6 h) or temperature (300 °C, 3 h) increases uniformity, as can be seen in the fitted nSLD profile without a higher-nSLD region near the substrate/film interface, Fig. 3(f). The optimal (290 °C, 6 h) sample exhibits slight reconstruction at the surface. This feature does not recur in a second, higher quality (i.e., lower resistance) sample from a more optimized growth (growth B). Figure 3(g) shows nSLD profiles from pieces of growth B in the as-grown and optimally reduced (290 °C, 6 h) state. The reduced $NdNiO_2$ film is uniform with a slightly higher nSLD than the previous samples, but still well below the calculated value. These data show that higher uniformity and reduced defect density can be pursued by optimization of both reduction conditions and of parent film synthesis. Of course, given that ion mobility may be altered by variations in defect density, these two factors may be coupled, with differing film quality resulting in changes to the optimal treatments.

V. DEFECTS AND HYDROGEN

We now examine the possibility that the nSLD suppression observed in even the most uniform, optimized samples could result from hydrogen incorporation, a longstanding controversy in CaH_2-reduced square-planar nickelates [39,42–45]. Given the wide range of hydrogen depth profiles reported in

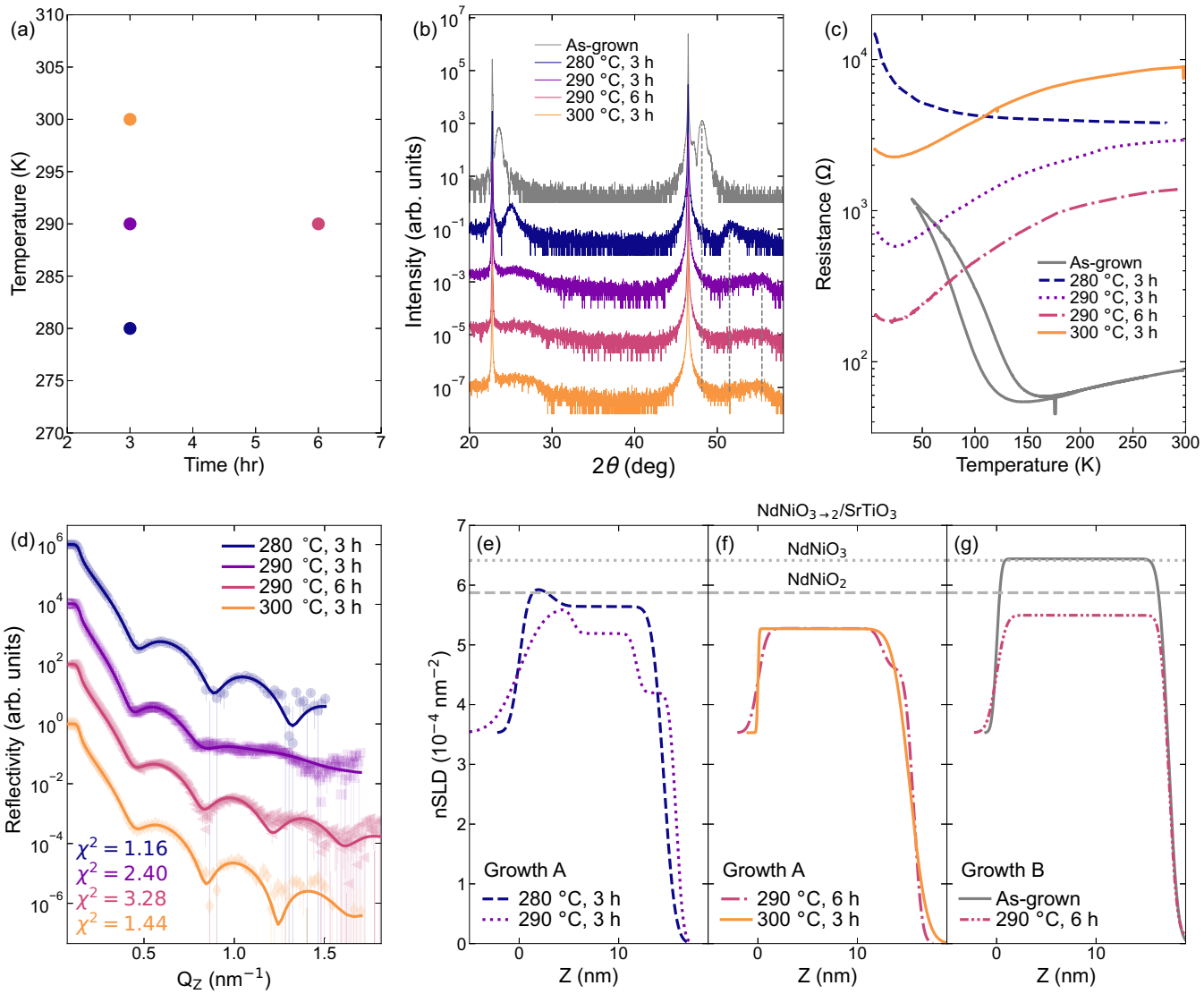

FIG. 3. (a) Schematic of thermal/temporal phase space for $NdNiO_{3\rightarrow 2}$ samples grown on $SrTiO_3$. (b) XRD symmetric scan from a $NdNiO_3$ film grown on $SrTiO_3$ which has been cleaved and reduced for a range of temperatures between 280 and 300 °C for 3–6 h. (c) Resistance vs temperature from the same films. (d) Neutron reflectometry and theoretical fits for all reduced films from growth A. (e) and (f) The best-fit nSLD profiles for the growth A films. (g) Best-fit nSLD profile for $NdNiO_3$ growth B samples before and after reduction to $NdNiO_2$ at 290 °C for 6 h. The gray dotted (dashed) lines represent the ideal bulk nSLD of $NdNiO_3$ ($NdNiO_2$).

the literature, we distinguish environmental hydrogen from reduction-incorporated hydrogen using deuterated $Ca(^2H)_2$, i.e., calcium deuteride or CaD_2. We reduced 10 nm and 15 nm thick $NdNiO_2$ films on $SrTiO_3$ via CaD_2 annealing for 3 h at 290 °C. This treatment condition [Fig. 3(e)] leads to a higher nSLD region near the substrate/film interface, approaching the expected theoretical nSLD of $NdNiO_2$. After reduction, samples were isolated in either vacuum or an inert He-gas environment, to minimize hydrogen/deuterium exchange, until being measured by SIMS 42 days later. After this first measurement, samples were exposed to atmosphere for approximately 80 days and remeasured.

Figures 4(a) and 4(b) show SIMS intensity profiles for selected ions from both films. All signals are normalized to the steady-state TiO_2^- intensity in the substrate to account for beam current fluctuations over multiple analyses. We define the interface of a given species as the point where it reaches 50% of the maximum intensity, and sputter depth increasing from right to left. As shown in Figs. 4(a) and 4(b), the D^- intensity is approximately an order of magnitude lower than H^-, implying that most studies examining hydrogen incorporation are measuring absorbed water, residual H gas in the chamber, or adsorbates such as surface hydrocarbons. The D^- intensity profiles show that the relative concentration of deuterium is highest near the surface of the film and decays to 50% of the maximum within a few nm. The intensity is significantly lower at the substrate/film interface, suggesting that for both the 10 nm and 15 nm films there is little to no D intercalation to the bottom of the film. Within the $SrTiO_3$, there is negligible D, and any visible intensity is likely due to an ion bombardment artifact in which the atoms are knocked into the substrate.

After aging, the H^- intensity increases near the film surface, consistent with the buildup of environmental adsorbates.

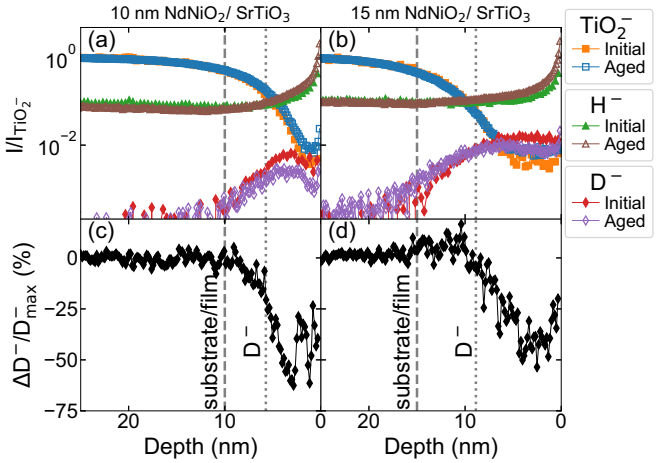

FIG. 4. (a) and (b) SIMS depth profiles showing the intensity of the TiO_2^-, H^-, and D^- ions for 10 nm (a) and 15 nm (b) thick $NdNiO_2$ films grown on $SrTiO_3$ and reduced by CaD_2 for 3 h at 290 °C. The sputtered depth increases from right to left (i.e., the surface of the film is at 0 nm). Aged data taken after 80 days of atmospheric exposure. (c) and (d) Reduction in D^- signal with aging, plotted as a percentage of the maximum D^- intensity in the initial state. The 10 nm film is shown in (c) and the 15 nm film is shown in (d).

In contrast, the D^- intensity decreases, as shown in Figs. 4(c) and 4(d), where the change in D^- intensity after aging is plotted as a percentage of the initial peak value. Interestingly, the H^- intensities for the the initial and aged samples converge near the 50% D^- position (i.e., the D^- "interface"). Given the increase in H^- intensity and the decrease in D^-, we attribute the reduction in D content to hydrogen/deuterium exchange. This process is confined to the upper region of the film and occurs slowly, with at least half of the initial D^- remaining in both films after 80 days. The slow exchange rate implies that the deuterium left behind by the reduction process is tightly bound, supporting a picture in which H or D acts as a compensation mechanism for charged defects. Recent work has found incomplete reduction to be associated with increased H content, again pointing towards compensation of charged defects [51]. The lack of residual D near the substrate/film interface then indicates a dramatically lower incidence of defects in this region of the reduced film, consistent with the various NR measurements showing a region of higher nSLD (i.e., closer to the theoretical value) near the bottom of the film. Regardless, the D^- intensities are vanishingly small, conclusively demonstrating that CaH_2 reduction does not meaningfully intercalate hydrogen.

In the context of nSLD values extracted from NR data, it is important to evaluate the potential effect of atmospheric hydrogen on the extracted values. Here we note that recent works have calculated the upper bound of hydrogen content to be in the range of 0.4 at% [42], 1.2 at% [44], and 0.2 at% [51]. At such concentrations, nSLD changes will be negligible, and minimal impact is expected on the band structure [52]. Further, multiple studies note similar hydrogen concentrations in the as-grown perovskite films, reduced infinite layer films, and substrates [42–44]. Throughout this work, the as-grown perovskite films and substrates are well described by ideal bulklike nSLDs, providing confirmation that the effects of absorbed atmospheric hydrogen are too small to alter nSLD values.

VI. STRAIN TUNING AND THERMAL STABILITY

In the absence of intercalated H, the observed nSLD suppression most likely indicates defective amorphous regions. Many infinite-layer nickelates are reduced at temperatures where they are metastable or near their decomposition temperatures, and are thought to be stabilized through substrate-induced strain [21,53,54]. In such a condition, extended defects in the parent film can act as nucleation sites for reduction-induced amorphization or disorder.

To test the impacts of epitaxial strain, we perform NR and XRR on two members of the RP $Nd_{n+1}Ni_nO_{3n+1}$ family reduced to the multilayer square-planar $Nd_{n+1}Ni_nO_{2n+2}$ phases, $n = 3$ and $n = 5$, across various strain states. These compounds are chosen due to their higher predicted stability at the relevant reduction temperatures, allowing us to better isolate the effects of substrate strain while minimizing temperature-induced amorphization [53,55]. $Nd_6Ni_5O_{12}$ superconducts, with a Ni $3d^{8.8}$ electron configuration ideally located in the nickelate superconducting dome [8]. In contrast, $Nd_4Ni_3O_8$ (Ni $3d^{8.67}$) is considered overdoped and manifests as a nonsuperconducting metal [21,56]. The NR data for these samples were corefined with XRR due to the low nSLD contrast between $Nd_4Ni_3O_8$ and certain substrates, as illustrated by Fig. 5(a). All samples were reduced at 290 °C for 6 h.

$Nd_6Ni_5O_{16\to12}$ films grown on $SrTiO_3$ are nearly lattice matched in the multilayered square-planar phase, but experience high tensile strain in the parent RP compound [21]. The high tensile strain of as-grown films promotes a high-concentration of misaligned, vertical rock-salt NdO defects (nSLD $= 3.34 \times 10^{-4}$ nm^{-2}) during growth [21], consistent with the suppressed as-grown nSLD shown in Fig. 5(b). Although the reduced phase, $Nd_6Ni_5O_{12}$, theoretically experiences minimal strain (0.13%), the high defect concentrations in the as-grown parent phase prevent a full topotactic transformation. This is reflected in the x-ray diffraction measurements shown in Fig. S4 [47], where only a small shift is observed in the film peak position.

Despite the partial transformation apparent in x-ray diffraction, the nSLD profile of the reduced film is suppressed relative to the theoretical value for $Nd_6Ni_5O_{12}$. Coupled with the reduced diffraction peak intensity, these results suggest that defects in the parent film induced by tensile strain promote amorphization upon reduction.

To probe the effects of high compressive strain, we measured $Nd_4Ni_3O_{10\to8}$ grown on $LaAlO_3$. While the parent RP phase is well-lattice matched to the substrate, the high compressive strain (>3%) imposed on the reduced square-planar phase is accompanied by a suppressed nSLD as shown in Fig. 5(c). The suppression is most severe near the substrate/film interface, consistent with our previous identification of a chemically distinct region at this interface. This result suggests strain effects may be most prominent in the region closest to the substrate. The portion of the film farthest from the substrate may partially relax, thus effectively experiencing lower strain and forming more crystalline $Nd_4Ni_3O_8$.

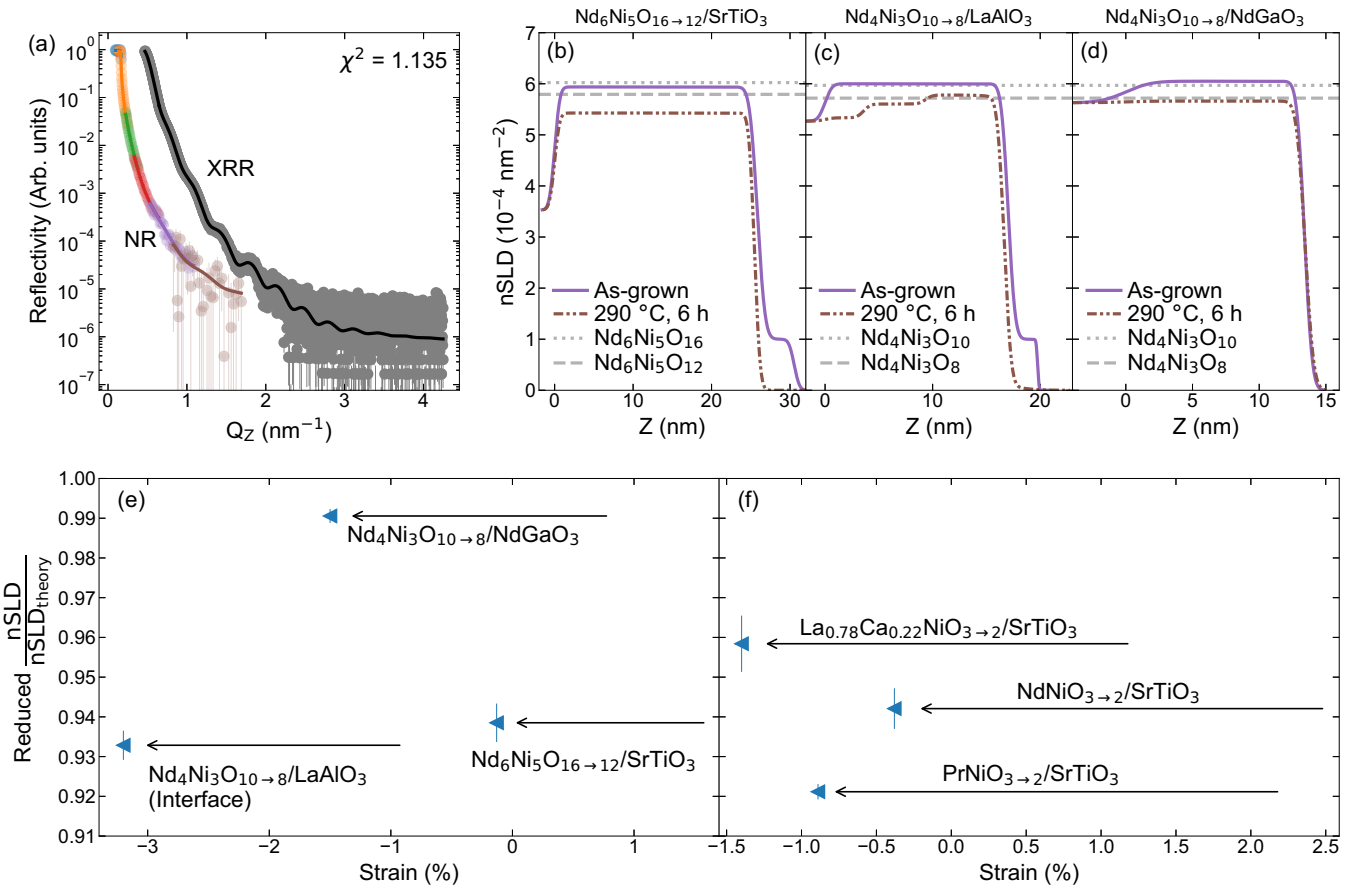

FIG. 5. (a) Example of corefined NR and XRR data to a coupled model showing data and theoretical fits. Gray circles are XRR data while the colored circles are NR data, with each color representing data from a single scattering angle. (b)–(d) nSLD profiles for square-planar nickelates under varying amounts of epitaxial strain before and after reduction: (b) $Nd_6Ni_5O_{16\rightarrow12}$ on $SrTiO_3$, (c) $Nd_4Ni_3O_{10\rightarrow8}$ on $LaAlO_3$, and (d) $Nd_4Ni_3O_{10\rightarrow8}$ on $NdGaO_3$. (e) and (f) Summary of the evolution and resulting ratio between theoretical and experimental nSLD values for (e) the RP → square-planar transformation and (f) the perovskite → infinite-layer transformations. Arrows are used to indicate initial strain in the as-grown phase, but do not represent the as-grown nSLD. The interfacial value was used for $Nd_4Ni_3O_{10\rightarrow8}/LaAlO_3$

$Nd_4Ni_3O_{10\rightarrow8}$ films grown on $NdGaO_3$ occupy a middle ground in which both the as-grown and reduced compounds experience moderate strain, and yield a uniform nSLD profile matching the theoretically expected value [Fig. 5(d)]. This matches previous observations that $NdGaO_3$ is an ideal substrate for the growth of $Nd_4Ni_3O_{10\rightarrow8}$ [21]. The results of the strain evolution are summarized in Fig. 5(e), which shows the ratio of the experimental and theoretical nSLD values for films on all three substrates.

For comparison, we plot similar results for the infinite layer compounds in Fig. 5(f). While the infinite-layer samples were all grown on $SrTiO_3$ and span a much smaller range of strain values, we note that the highest ratio of the theoretical and experimental nSLDs is found in $La_{0.78}Ca_{0.22}NiO_2$, which is the closest match to the strain state in $Nd_4Ni_3O_{10\rightarrow8}/NdGaO_3$. $La_{0.78}Ca_{0.22}NiO_2$ further exhibited a large region of vertical uniformity in the 25 nm thick sample, possibly supported by this strain condition. Even so, $La_{0.78}Ca_{0.22}NiO_2$ is less stable at reduction temperatures than $Nd_4Ni_3O_8$, leading to significant surface reconstruction.

Due to the dramatic expansion of the in-plane lattice upon reduction, it is not possible to choose a substrate which is well-lattice matched to both the as-grown and square-planar phases. Despite this intrinsic challenge, these results suggest that by optimizing epitaxial strain and synthesizing compounds with higher chemical stability, layered nickelate films of high crystallinity and uniformity can be achieved.

VII. DISCUSSION AND CONCLUSIONS

Our experiments examine the interplay between reduction conditions, strain, and material stability in determining the depth profile of square-planar nickelates, pointing to key factors controlling the resultant depth profile. The surface reconstructions, interface effects and nSLD suppression observed in reduced nickelate films show that the growing concerns [51] regarding amorphization are well founded. SIMS measurements confirm that the nSLD suppression is not the result of H-intercalation—the most likely explanation is the formation of low-density amorphous regions within the reduced films, which evade detection via x-ray diffraction and electrical transport measurements.

One important factor is the influence of strain effects on the chemistry at the interface. While SIMS shows the $NdNiO_3/SrTiO_3$ interface to be effectively D-free, we find trace amounts of trapped D near the surface, presumably

acting as a charge compensator in more defective regions. Many infinite-layer films exhibit higher-nSLD regions at the substrate/film interface, particularly in samples which evolve from moderate tensile strain in the parent compound to an excellent lattice match in the reduced phase. Increasing the reduction time and/or temperature may achieve a more uniform depth profile at the cost of increased amorphization. Further complicating optimization is the tendency for high-temperature reductions to display surface reconstruction, so that only a narrow temperature window exists in which the interface is fully reduced and the surface is not yet degraded.

To widen and access this window, we can optimize strain and reduce films with higher thermal stability. For example, the depth profile of $Nd_4Ni_3O_8/NdGaO_3$ is uniform with ideal nSLD value. The strain state of $Nd_4Ni_3O_8/NdGaO_3$ evolves from moderate tension in the precursor phase to moderate compression after reduction, while the increased thermal stability of $Nd_4Ni_3O_8$ inhibits amorphization. Still, nonuniformity may be induced by strain even in $Nd_4Ni_3O_8$, and $Nd_4Ni_3O_8/LaAlO_3$ exhibits mild nSLD suppression at the film substrate interface due to the large compression of the square-planar phase. Thus, by synthesizing layered nickelates on substrates spanning a variety of strain states, we identify that in both the infinite- and multilayer square-planar nickelates, avoiding excessive strain in both the as-grown and reduced phase yields films with higher density, while films with higher thermal stability are more resistant to amorphization.

These experiments demonstrate that the reduction of each nickelate/substrate pair must be approached as a unique system. Reduction affects surface, bulk and substrate/film interface regions differently, while strain, reduction temperature, reduction time, and the stability of the individual square-planar structure all strongly influence the resulting depth profile. Conditions which limit amorphization may not fully reduce the film substrate interface, while a uniform depth profile may be associated with significant amorphization, pointing towards competition between crystal quality and vertical uniformity.

The large deviations from ideal nSLD values present in most films indicate that volume-averaged probes are likely relying on inaccurate estimates of the superconducting volume fraction, a critical factor for accurately extracting physical parameters in the superconducting state. We emphasize that this work focuses on samples without capping layers. Such uncapped samples are extensively studied and have been shown to superconduct regularly [6,8,39,42,51,56–58]. However, additional neutron reflectometry studies on capped samples are clearly warranted to examine possible routes towards limiting amorphization. Only by carefully understanding the interplay among many complex factors can we move toward reproducible high-quality superconducting nickelate films.

VIII. EXPERIMENTAL METHODS

A. Sample synthesis

1. $La_{1-x}(Ca,Sr)_xNiO_2$ *films*

The $La_{0.78}Ca_{0.22}NiO_3$ and $La_{0.78}Ca_{0.22}NiO_2$ films were grown on $SrTiO_3$ (001) substrates using pulsed laser deposition (PLD) and CaH_2 topotactic reduction [59,60]. $SrTiO_3$ (001) substrates were etched with hydrofluoric acid and annealed in air at 900 °C for 90 min before deposition. This is to maximize the TiO_2 termination which serves to minimize disordered Ruddlesden-Popper type growth. We first grow the perovskite phase using PLD with the following optimal set of parameters: $T_{growth} = 575$ °C, $P_{O_2} = 19.99$ Pa (150 mTorr), $J = 2.5\,J/cm^2$. Afterwards, the film was postannealed at growth temperature under the same oxygen partial pressure for 10 min followed by cooling at 8 °C min^{-1}. The topotactic phase transition to infinite-layer phase was mediated by the substrate strain and performed in the same PLD vacuum chamber with a base pressure of less than 133 μPa. The reduction environment was achieved by heating approximately 0.1 g of CaH_2 powder to obtain a (H_2 and other species) pressure in the range approximately 13 to 40 Pa. Samples are annealed at 340 °C for 1 h.

2. $Nd_4Ni_3O_{10}$, $Nd_6Ni_5O_{12}$, *and* $NdNiO_2$ *films*

We use ozone-assisted molecular beam epitaxy (MBE) to synthesize the precursor $NdNiO_3/SrTiO_3$ (001), $Nd_4Ni_3O_{10}/LaAlO_3$ (001), $Nd_4Ni_3O_{10}/NdGaO_3$ (110), and $Nd_6Ni_5O_{16}/SrTiO_3$ (001) films. To calibrate the nickel and neodymium elemental fluxes, we synthesize NiO on MgO (001) and Nd_2O_3 on yttria-stabilized zirconia (YSZ) (111), then measure the film thickness via x-ray reflectivity. Next, we synthesize $NdNiO_3/LaAlO_3$ (001) and use the *c*-axis lattice constant and film thickness to refine the Nd / Ni ratio and monolayer dose, respectively. Using the optimized neodymium and nickel shutter times from the synthesis of $NdNiO_3/LaAlO_3$, we synthesize the Ruddlesden-Popper nickelates via monolayer shuttering. Both $NdNiO_3$ and Ruddlesden-Popper nickelates are synthesized at substrate temperatures of 500 to 600 °C with approximately 133 μPa distilled ozone (Heeg Vacuum Engineering). The MBE synthesis conditions and calibration scheme are described in Refs. [8,21,24]; similar techniques were also used in Refs. [61,62].

The perovskite and Ruddlesden-Popper films are reduced to the square-planar phase via CaH_2 topotactic reduction. The following methods are similar to those used elsewhere [8,22,25]. First, the as-grown films are cut into identical pieces, and the pieces to be reduced are loosely wrapped in aluminum foil (All-Foils) to avoid direct contact between the film and CaH_2. Each film is then placed in a borosilicate tube (Chemglass Life Sciences) with approximately 0.1 g of CaH_2 pieces (> 92%, Alfa Aesar). The borosilicate tube is pumped down to < 67 mPa, sealed, and then heated for several hours at 290 °C in a convection oven (Heratherm, Thermo Fisher Scientific) with a 10 °C min^{-1} heating rate.

3. $Nd_{0.8}Sr_{0.2}NiO_3$ *films*

Polycrystalline targets of $Nd_{0.8}Sr_{0.2}NiO_3$ were prepared by the liquid-mix technique [63,64]. 10 nm thick $Nd_{0.8}Sr_{0.2}NiO_3$ films were grown on (001) $SrTiO_3$ substrates using a Neocera PLD system equipped with an *in-situ* RHEED (Staib Instruments, Germany). The depositions were conducted using a KrF excimer laser operating at 2 Hz with a fluence of 1.5 J cm^{-2}. During the deposition, a dynamic oxygen pressure of 20 Pa was maintained, and the substrate temperature was 735 °C. The optional 10 nm thick $SrTiO_3$ capping layer was

grown at the same condition as the film. After the deposition, all samples were *in-situ* annealed at the deposition temperature in an oxygen atmosphere of 67 kPa for 30 min and subsequently cooled to room temperature at a rate of 15 °C min^{-1}.

The as-grown films were sealed in evacuated (approximately 133 mPa) quartz ampoules with 0.1 g CaH_2 powder (90%–95%, Thermo Scientific Chemicals). The ampoules were then baked in a muffle furnace at 600 °C for up to 10 h. The temperature ramp rate was fixed at 10 °C min^{-1}. Once the ampoules were opened, the reduced films were immediately rinsed in *n*-butanol and isopropanol in an ultrasonic bath for 3 min.

B. X-ray diffraction

X-ray diffraction (XRD) measurements were performed at room temperature before and after reduction by each group on commercially available x-ray diffractometers using Cu Kα_1 ($\lambda = 1.5406$ Å) radiation.

C. Reflectometry

1. X-ray reflectometry

X-ray reflectometry (XRR) measurements were performed at ambient conditions in a horizontal configuration using a Rigaku SmartLab diffractometer. The incident beam was collimated using the parallel beam slit and an incident slit of 30 μm height to improve Q_Z-resolution. The Cu Kα_1 wavelength ($\lambda = 1.5406$ Å) was isolated by using a Ge-(220)×2 monochromator. The scattered beam was further collimated by a 0.2 mm receiving slit. The data were reduced using the *reductus* web service [65] and fit to a slab model using Refl1D [66].

2. Neutron reflectometry

Unpolarized neutron reflectometry (NR) measurements were performed on multiple instruments: the Polarized Beam Reflectometer (PBR) and CHRNS-CANDOR White-Beam Reflectometer at the NIST Center for Neutron Research (NCNR), the Beamline 4A Magnetism Reflectometer (MAGREF or BL-4A) at the Spallation Neutron Source, Oak Ridge National Laboratory and the Polref instrument at the ISIS Neutron and Muon Source, Rutherford Appleton Laboratory, UK. All measurements were performed using unpolarized neutrons in ambient temperature and pressure.

On PBR, a monochromated neutron beam of wavelength $\lambda = 4.75$ Å and pencil detector were used, while on CANDOR, a polychromatic beam (4 to 6 Å) was used with 54 individual detectors to perform wavelength analysis. Reflectivities $R(\lambda, \theta)$ were taken at many different angles θ and combined using the relation $Q = 4\pi \sin(\theta)/\lambda$ using the *reductus* web service [65]. On BL-4A, a polychromatic beam (4.5 to 10.5 Å) pulsed at 30 Hz was used, with wavelength analyzed by time-of-flight into 250 wavelength bands. The 2D detector allowed simultaneous measurement of multiple small-area samples in addition to measurement of multiple reflection angles θ at each discrete motor angle setting. The resulting curves $R(Q)$ taken at each angle were reduced separately and fit simultaneously to allow correction for small motor misalignments. Polref is a polychromatic beam machine (1 to 14 Å) pulsed at 10 Hz, three angles were used to obtain the full Q range. Data was reduced using a Jupyter notebook with the imported Mantid API. Finally, all NR data were fit using the Refl1D software package to simulate reflectivity from defined slab models [66].

D. Time-of-flight secondary ion mass spectroscopy

Time-of-flight SIMS was performed using an IONTOF IV (Münster, Germany) equipped with a 20 keV $Ar^+_{2600\pm1000}$ cluster source for sputtering, a 30 keV Bi_3^+ liquid metal ion source for analysis, and a time-of-flight mass analyzer. Depth profiling was performed in noninterlaced mode with 1 scan of analysis with a lateral resolution of (128 × 128) pixels, 10 scans of sputtering, and at least 0.5 s of charge compensation per cycle. The corresponding ion doses were 1.9×10^9 ions/cm^2 (0.12 pA) for Bi_3^+, and between 2.1×10^{14} ions/cm^2 to 2.6×10^{14} ions/cm^2 (5.1 to 6.4 nA) per cycle for the cluster source due to day-to-day fluctuations in the beam current. To improve charge compensation on insulating substrates, conductive tape was used to connect a corner of the film surface to the sample holder. For reliable detection of H^- and D^- ions, contributions from residual gases were minimized by keeping the chamber pressure below 5×10^{-7} Pa.

Spectra were analyzed using SurfaceLab to define a region of interest, perform mass calibrations, identify peaks with the appropriate compounds, and extract the total integrated peak intensity as a function of sputter time. As many molecular compounds can have similar mass, peak assignments were made carefully, considering factors such as mass offset, isotopic distribution, and similarity in profile shape to other known oxide and hydroxide species.

E. Electrical transport

Electrical transport measurements in Fig. 3 were taken using a home-built electrical 'dipstick probe' compatible with a helium dewar. Indium contacts were soldered on the four corners of each sample in a Van der Pauw configuration. AC transport measurements were taken at 17.777 Hz using an SR-830 lock-in amplifier. The voltage and current were measured simultaneously to determine the resistance.

ACKNOWLEDGMENTS

M.B.-S., D.F.S., G.A.P., and J.A.M. acknowledge support from the U.S. Department of Energy, Office of Basic Energy Sciences, Division of Materials Sciences and Engineering, under Award No. DE-SC0021925. J.A.M. acknowledges support from NSF Grant No. DMR-2323971. L.E.C., Z.L., and A.A. acknowledge support from the Ministry of Education (MOE), Singapore, under its Tier-2 Academic Research Fund (AcRF), Grant No. MOE-T2EP50123-0013, the MOE Tier-3 Grant (MOE-MOET32023-0003) 'Quantum Geometric Advantage', and the SUSTech-NUS Joint Research Program. J.R. and M.S. acknowledge support from an ARO MURI program with Award No. W911NF-21-1-0327, and the National Science Foundation of the U.S. under Grant No. DMR-2122071. R.K.P. and S.M. acknowledge funding support from a SERB (ANRF) Core Research grant: No. CRG/2022/001906 and I.R.H.P.A Grant No. IPA/2020/000034. Materials growth

was supported in part by PARADIM under NSF Cooperative Agreement No. DMR-2039380.

P.P.B. and P.Q. received funding from the NRC RAP. G.A.P. acknowledges additional support from the Paul and Daisy Soros Fellowship for New Americans. D.F.S. and G.A.P. acknowledge support from the NSF Graduate Research Fellowship Grant No. DGE-1745303. M.B.S. acknowledges support from the NSF Graduate Research Fellowship Grant No. DGE-2141064.

We would like to thank the ISIS neutron and Muon Source for the provision of beamtime RB2320137. The data is available at the following [67]. A portion of this research used resources at the Spallation Neutron Source, a DOE Office of Science User Facility operated by the Oak Ridge National Laboratory. The beam time was allocated to Magnetism Reflectometer (BL4A) on Proposal No. IPTS-29514.

Access to CANDOR was provided by the Center for High Resolution Neutron Scattering, a partnership between the National Institute of Standards and Technology and the National Science Foundation under Agreement No. DMR-2010792. Research was performed in part at the NIST Center for Nanoscale Science and Technology. Certain commercial equipment, instruments, software, or materials are identified in this paper in order to specify the experimental procedure adequately. Such identifications are not intended to imply recommendation or endorsement by NIST, nor it is intended to imply that the materials or equipment identified are necessarily the best available for the purpose. Unless otherwise noted, NIST work was funded solely by the U.S. Government.

DATA AVAILABILITY

Some of the data that support the findings of this article are openly available [67]. Other datasets are not publicly available upon publication because it is not technically feasible and/or the cost of preparing, depositing, and hosting the data would be prohibitive within the terms of this research project. The data are available from the authors upon reasonable request.

[1] J. Chaloupka and G. Khaliullin, Orbital order and possible superconductivity in $LaNiO_3/LaMO_3$ superlattices, Phys. Rev. Lett. **100**, 016404 (2008).

[2] V. I. Anisimov, D. Bukhvalov, and T. M. Rice, Electronic structure of possible nickelate analogs to the cuprates, Phys. Rev. B **59**, 7901 (1999).

[3] D. Li, K. Lee, B. Y. Wang, M. Osada, S. Crossley, H. R. Lee, Y. Cui, Y. Hikita, and H. Y. Hwang, Superconductivity in an infinite-layer nickelate, Nature (London) **572**, 624 (2019).

[4] M. Osada, B. Y. Wang, B. H. Goodge, K. Lee, H. Yoon, K. Sakuma, D. Li, M. Miura, L. F. Kourkoutis, and H. Y. Hwang, A superconducting praseodymium nickelate with infinite layer structure, Nano Lett. **20**, 5735 (2020).

[5] M. Osada, B. Y. Wang, B. H. Goodge, S. P. Harvey, K. Lee, D. Li, L. F. Kourkoutis, and H. Y. Hwang, Nickelate superconductivity without rare-earth magnetism: (La, Sr)NiO_2, Adv. Mater. **33**, 2104083 (2021).

[6] S. Zeng, C. Li, L. E. Chow, Y. Cao, Z. Zhang, C. S. Tang, X. Yin, Z. S. Lim, J. Hu, P. Yang, and A. Ariando, Superconductivity in infinite-layer nickelate $La_{1-x}Ca_xNiO_2$ thin films, Sci. Adv. **8**, eabl9927 (2022).

[7] W. Wei, D. Vu, Z. Zhang, F. J. Walker, and C. H. Ahn, Superconducting $Nd_{1-x}Eu_xNiO_2$ thin films using *in situ* synthesis, Sci. Adv. **9**, eadh3327 (2023).

[8] G. A. Pan, D. Ferenc Segedin, H. LaBollita, Q. Song, E. M. Nica, B. H. Goodge, A. T. Pierce, S. Doyle, S. Novakov, D. Córdova Carrizales, *et al.*, Superconductivity in a quintuple-layer square-planar nickelate, Nat. Mater. **21**, 160 (2022).

[9] H. Sahib, A. Raji, F. Rosa, G. Merzoni, G. Ghiringhelli, M. Salluzzo, A. Gloter, N. Viart, and D. Preziosi, Superconductivity in $PrNiO_2$ infinite-layer nickelates, Adv. Mater. **37**, 2416187 (2025).

[10] C. T. Parzyck, Y. Wu, L. Bhatt, M. Kang, Z. Arthur, T.-M. Pedersen, R. Sutarto, S. Fan, J. Pelliciari, V. Bisogni, *et al.*, Superconductivity in the parent infinite-layer nickelate $NdNiO_2$, Phys. Rev. X **15**, 021048 (2025).

[11] J. Fowlie, M. Hadjimichael, M. M. Martins, D. Li, M. Osada, B. Y. Wang, K. Lee, Y. Lee, Z. Salman, T. Prokscha, J.-M. Triscone, H. Y. Hwang, and A. Suter, Intrinsic magnetism in superconducting infinite-layer nickelates, Nat. Phys. **18**, 1043 (2022).

[12] K. Lee, B. Y. Wang, M. Osada, B. H. Goodge, T. C. Wang, Y. Lee, S. Harvey, W. J. Kim, Y. Yu, C. Murthy, S. Raghu, L. F. Kourkoutis, and H. Y. Hwang, Linear-in-temperature resistivity for optimally superconducting (Nd,Sr)NiO_2, Nature (London) **619**, 288 (2023).

[13] C. Lane, R. Zhang, B. Barbiellini, R. S. Markiewicz, A. Bansil, J. Sun, and J.-X. Zhu, Competing incommensurate spin fluctuations and magnetic excitations in infinite-layer nickelate superconductors, Commun. Phys. **6**, 90 (2023).

[14] S. L. E. Chow, Z. Luo, and A. Ariando, Bulk superconductivity near 40 K in hole-doped $SmNiO_2$ at ambient pressure, Nature (London) **642**, 58 (2025).

[15] H. Sun, M. Huo, X. Hu, J. Li, Z. Liu, Y. Han, L. Tang, Z. Mao, P. Yang, B. Wang, *et al.*, Signatures of superconductivity near 80 K in a nickelate under high pressure, Nature (London) **621**, 493 (2023).

[16] N. Wang, G. Wang, X. Shen, J. Hou, J. Luo, X. Ma, H. Yang, L. Shi, J. Dou, J. Feng, *et al.*, Bulk high-temperature superconductivity in pressurized tetragonal $La_2PrNi_2O_7$, Nature (London) **634**, 579 (2024).

[17] Y. Zhu, D. Peng, E. Zhang, B. Pan, X. Chen, L. Chen, H. Ren, F. Liu, Y. Hao, N. Li, *et al.*, Superconductivity in pressurized trilayer $La_4Ni_3O_{10-\delta}$ single crystals, Nature (London) **631**, 531 (2024).

[18] E. K. Ko, Y. Yu, Y. Liu, L. Bhatt, J. Li, V. Thampy, C.-T. Kuo, B. Y. Wang, Y. Lee, K. Lee, J.-S. Lee, B. H. Goodge, D. A. Muller, and H. Y. Hwang, Signatures of ambient pressure superconductivity in thin film $La_3Ni_2O_7$, Nature (London) **638**, 935 (2025).

[19] G. Zhou, W. Lv, H. Wang, Z. Nie, Y. Chen, Y. Li, H. Huang, W.-Q. Chen, Y.-J. Sun, Q.-K. Xue, and Z. Chen, Ambient-pressure superconductivity onset above 40 K in $(La, Pr)_3Ni_2O_7$ films, Nature (London) **640**, 641 (2025).

[20] X. Zhou, P. Qin, Z. Feng, H. Yan, X. Wang, H. Chen, Z. Meng, and Z. Liu, Experimental progress on the emergent

infinite-layer Ni-based superconductors, Mater. Today **55**, 170 (2022).

[21] D. Ferenc Segedin, B. H. Goodge, G. A. Pan, Q. Song, H. LaBollita, M.-C. Jung, H. El-Sherif, S. Doyle, A. Turkiewicz, N. K. Taylor, *et al.*, Limits to the strain engineering of layered square-planar nickelate thin films, Nat. Commun. **14**, 1468 (2023).

[22] K. Lee, B. H. Goodge, D. Li, M. Osada, B. Y. Wang, Y. Cui, L. F. Kourkoutis, and H. Y. Hwang, Aspects of the synthesis of thin film superconducting infinite-layer nickelates, APL Mater. **8**, 041107 (2020).

[23] C. T. Parzyck, V. Anil, Y. Wu, B. H. Goodge, M. Roddy, L. F. Kourkoutis, D. G. Schlom, and K. M. Shen, Synthesis of thin film infinite-layer nickelates by atomic hydrogen reduction: Clarifying the role of the capping layer, APL Mater. **12**, 031132 (2024).

[24] G. A. Pan, Q. Song, D. Ferenc Segedin, M.-C. Jung, H. El-Sherif, E. E. Fleck, B. H. Goodge, S. Doyle, D. Córdova Carrizales, A. T. N'Diaye, *et al.*, Synthesis and electronic properties of $Nd_{n+1}\,Ni_n\,O_{3n+1}$ Ruddlesden-Popper nickelate thin films, Phys. Rev. Mater. **6**, 055003 (2022).

[25] Y. Li, W. Sun, J. Yang, X. Cai, W. Guo, Z. Gu, Y. Zhu, and Y. Nie, Impact of cation stoichiometry on the crystalline structure and superconductivity in nickelates, Front. Phys. **9**, 719534 (2021).

[26] M. Kawai, S. Inoue, M. Mizumaki, N. Kawamura, N. Ichikawa, and Y. Shimakawa, Reversible changes of epitaxial thin films from perovskite $LaNiO_3$ to infinite-layer structure $LaNiO_2$, Appl. Phys. Lett. **94**, 082102 (2009).

[27] T. Onozuka, A. Chikamatsu, T. Katayama, T. Fukumura, and T. Hasegawa, Formation of defect-fluorite structured $NdNiO_xH_y$ epitaxial thin films via a soft chemical route from $NdNiO_3$ precursors, Dalton Trans. **45**, 12114 (2016).

[28] J. de Vries, G. Stollman, and M. Gijs, Analysis of the critical current density in high-T_c superconducting films, Phys. C **157**, 406 (1989).

[29] X.-R. Zhou, Z.-X. Feng, P.-X. Qin, H. Yan, X.-N. Wang, P. Nie, H.-J. Wu, X. Zhang, H.-Y. Chen, Z.-A. Meng, Z.-W. Zhu, and Z.-Q. Liu, Negligible oxygen vacancies, low critical current density, electric-field modulation, in-plane anisotropic and high-field transport of a superconducting $Nd_{0.8}Sr_{0.2}NiO_2/SrTiO_3$ heterostructure, Rare Metals **40**, 2847 (2021).

[30] I. Hetel, T. R. Lemberger, and M. Randeria, Quantum critical behavior in the superfluid density of strongly underdoped ultrathin copper oxide films, Nat. Phys. **3**, 700 (2007).

[31] K. Held, L. Si, P. Worm, O. Janson, R. Arita, Z. Zhong, J. M. Tomczak, and M. Kitatani, Phase diagram of nickelate superconductors calculated by dynamical vertex approximation, Front. Phys. **9**, 810394 (2022).

[32] A. Ikeda, T. Manabe, and M. Naito, Improved conductivity of infinite-layer $LaNiO_2$ thin films by metal organic decomposition, Phys. C **495**, 134 (2013).

[33] B. H. Goodge, B. Geisler, K. Lee, M. Osada, B. Y. Wang, D. Li, H. Y. Hwang, R. Pentcheva, and L. F. Kourkoutis, Resolving the polar interface of infinite-layer nickelate thin films, Nat. Mater. **22**, 466 (2023).

[34] R. He, P. Jiang, Y. Lu, Y. Song, M. Chen, M. Jin, L. Shui, and Z. Zhong, Polarity-induced electronic and atomic reconstruction at $NdNiO_2/SrTiO_3$ interfaces, Phys. Rev. B **102**, 035118 (2020).

[35] L. E. Chow and A. Ariando, Infinite-layer nickelate superconductors: a current experimental perspective of the crystal and electronic structures, Front. Phys. **10**, 834658 (2022).

[36] C. Yang, R. Pons, W. Sigle, H. Wang, E. Benckiser, G. Logvenov, B. Keimer, and P. A. van Aken, Direct observation of strong surface reconstruction in partially reduced nickelate films, Nat. Commun. **15**, 378 (2024).

[37] G. Krieger, A. Raji, L. Schlur, G. Versini, C. Bouillet, M. Lenertz, J. Robert, A. Gloter, N. Viart, and D. Preziosi, Synthesis of infinite-layer nickelates and influence of the capping-layer on magnetotransport, J. Phys. D **56**, 024003 (2022).

[38] S. Fan, H. LaBollita, Q. Gao, N. Khan, Y. Gu, T. Kim, J. Li, V. Bhartiya, Y. Li, W. Sun, *et al.*, Capping effects on spin and charge excitations in parent and superconducting $Nd_{1-x}Sr_xNiO_2$, Phys. Rev. Lett. **133**, 206501 (2024).

[39] X. Ding, C. C. Tam, X. Sui, Y. Zhao, M. Xu, J. Choi, H. Leng, J. Zhang, M. Wu, H. Xiao, *et al.*, Critical role of hydrogen for superconductivity in nickelates, Nature (London) **615**, 50 (2023).

[40] L. Si, W. Xiao, J. Kaufmann, J. M. Tomczak, Y. Lu, Z. Zhong, and K. Held, Topotactic hydrogen in nickelate superconductors and akin infinite-layer oxides ABO_2, Phys. Rev. Lett. **124**, 166402 (2020).

[41] L. Si, P. Worm, D. Chen, and K. Held, Topotactic hydrogen forms chains in ABO_2 nickelate superconductors, Phys. Rev. B **107**, 165116 (2023).

[42] P. P. Balakrishnan, D. Ferenc Segedin, L. E. Chow, P. Quarterman, S. Muramoto, M. Surendran, R. K. Patel, H. LaBollita, G. A. Pan, Q. Song, *et al.*, Extensive hydrogen incorporation is not necessary for superconductivity in topotactically reduced nickelates, Nat. Commun. **15**, 7387 (2024).

[43] S. Zeng, C. S. Tang, Z. Luo, L. E. Chow, Z. S. Lim, S. Prakash, P. Yang, C. Diao, X. Yu, Z. Xing, *et al.*, Origin of a topotactic reduction effect for superconductivity in infinite-layer nickelates, Phys. Rev. Lett. **133**, 066503 (2024).

[44] M. Gonzalez, A. Ievlev, K. Lee, W. Kim, Y. Yu, J. Fowlie, and H. Y. Hwang, Absence of hydrogen insertion into highly crystalline superconducting infinite layer nickelates, Phys. Rev. Mater. **8**, 084804 (2024).

[45] J. Nie, X. Chen, Y. Bian, X. Wang, T. Shao, J. Gao, W. Mao, B. Ge, A. Müller, and J. Chen, Irrelevance of ^{1}H composition to superconductivity in infinite-layer nickelates from measurements of nuclear interactions, Newton **1**, 100006 (2025).

[46] P. A. Kienzle, B. B. Maranville, K. V. O'Donovan, J. F. Ankner, N. F. Berk, and C. F. Majkrzak, Refl1d, https://www.nist.gov/ncnr/reflectometry-software (2017).

[47] See Supplemental Material at http://link.aps.org/supplemental/10.1103/9ldc-sk6x for tables of sample structural properties and scattering length densities, additional x-ray diffraction, additional neutron and x-ray reflectometry scattering and analysis, and additional secondary ion mass spectrometry data.

[48] P. Puphal, Y.-M. Wu, K. Fürsich, H. Lee, M. Pakdaman, J. A. N. Bruin, J. Nuss, Y. E. Suyolcu, P. A. van Aken, B. Keimer, M. Isobe, and M. Hepting, Topotactic transformation of single crystals: From perovskite to infinite-layer nickelates, Sci. Adv. **7**, eabl8091 (2021).

[49] Q. Li, C. He, J. Si, X. Zhu, Y. Zhang, and H.-H. Wen, Absence of superconductivity in bulk $Nd_{1-x}Sr_xNiO_2$, Commun. Mater. **1**, 16 (2020).

[50] J. García-Muñoz, M. Suaaidi, M. Martínez-Lope, and J. Alonso, Influence of carrier injection on the metal-insulator transition in electron-and hole-doped $R_{1-x}A_xNiO_3$ perovskites, Phys. Rev. B **52**, 13563 (1995).

[51] Y. Li, C. Liu, H. Zheng, J. S. Jiang, Z. Zhu, X. Yan, H. Cao, K. V. L. V. Narayanachari, B. Paudel, K. P. Koirala, *et al.*, On the topotactic phase transition achieving superconducting infinite-layer nickelates, Adv. Mater. **36**, 2402484 (2024).

[52] S. Di Cataldo, P. Worm, L. Si, and K. Held, Absence of electron-phonon-mediated superconductivity in hydrogen-intercalated nickelates, Phys. Rev. B **108**, 174512 (2023).

[53] M. Hayward, M. Green, M. Rosseinsky, and J. Sloan, Sodium hydride as a powerful reducing agent for topotactic oxide deintercalation: synthesis and characterization of the nickel (i) oxide $LaNiO_2$, J. Am. Chem. Soc. **121**, 8843 (1999).

[54] M. Hayward and M. Rosseinsky, Synthesis of the infinite layer Ni (I) phase $NdNiO_{2+x}$ by low temperature reduction of $NdNiO_3$ with sodium hydride, Solid State Sci. **5**, 839 (2003).

[55] P. Lacorre, Passage from T-type to T'-type arrangement by reducing $R_4Ni_3O_{10}$ to $R_4Ni_3O_8$ (R= La, Pr, Nd), J. Solid State Chem. **97**, 495 (1992).

[56] S. Zeng, C. S. Tang, X. Yin, C. Li, M. Li, Z. Huang, J. Hu, W. Liu, G. J. Omar, H. Jani, *et al.*, Phase diagram and superconducting dome of infinite-layer $Nd_{1-x}Sr_xNiO_2$ thin films, Phys. Rev. Lett. **125**, 147003 (2020).

[57] M. Xu, Y. Zhao, Y. Chen, X. Ding, H. Leng, Z. Hu, X. Wu, J. Yi, X. Yu, M. B. H. Breese, S. Xi, M. Li, and L. Qiao, Robust superconductivity in infinite-layer nickelates, Adv. Sci. **11**, 2305252 (2024).

[58] X. Ding, S. Shen, H. Leng, M. Xu, Y. Zhao, J. Zhao, X. Sui, X. Wu, H. Xiao, X. Zu, *et al.*, Stability of superconducting $Nd_{0.8}Sr_{0.2}NiO_2$ thin films, Sci. China Phys. Mech. Astron. **65**, 267411 (2022).

[59] L. E. Chow, S. Kunniniyil Sudheesh, Z. Y. Luo, P. Nandi, T. Heil, J. Deuschle, S. W. Zeng, Z. T. Zhang, S. Prakash, X. M. Du, *et al.*, Pairing symmetry in infinite-layer nickelate superconductor, arXiv:2201.10038.

[60] L. E. Chow, K. Y. Yip, M. Pierre, S. W. Zeng, Z. T. Zhang, T. Heil, J. Deuschle, P. Nandi, S. K. Sudheesh, Z. S. Lim, *et al.*, Pauli-limit violation in lanthanide infinite-layer nickelate superconductors, arXiv:2204.12606.

[61] Z. Li, W. Guo, T. T. Zhang, J. H. Song, T. Y. Gao, Z. B. Gu, and Y. F. Nie, Epitaxial growth and electronic structure of Ruddlesden–Popper nickelates ($La_{n+1}Ni_nO_{3n+1}$, $n = 1$–5), APL Mater. **8**, 091112 (2020).

[62] W. Sun, Y. Li, X. Cai, J. Yang, W. Guo, Z. Gu, Y. Zhu, and Y. Nie, Electronic and transport properties in Ruddlesden-Popper neodymium nickelates $Nd_{n+1}Ni_nO_{3n+1}$ (n=1–5), Phys. Rev. B **104**, 184518 (2021).

[63] R. K. Patel, K. Patra, S. K. Ojha, S. Kumar, S. Sarkar, A. Saha, N. Bhattacharya, J. W. Freeland, J.-W. Kim, P. J. Ryan, P. Mahadevan, and S. Middey, Hole doping in a negative charge transfer insulator, Commun. Phys. **5**, 216 (2022).

[64] R. K. Patel, S. K. Ojha, S. Kumar, A. Saha, P. Mandal, J. W. Freeland, and S. Middey, Epitaxial stabilization of ultra thin films of high entropy perovskite, Appl. Phys. Lett. **116**, 071601 (2020).

[65] B. Maranville, W. Ratcliff II, and P. Kienzle, *reductus*: a stateless Python data reduction service with a browser front end, J. Appl. Cryst. **51**, 1500 (2018).

[66] B. J. Kirby, P. A. Kienzle, B. B. Maranville, N. F. Berk, J. Krycka, F. Heinrich, and C. F. Majkrzak, Phase-sensitive specular neutron reflectometry for imaging the nanometer scale composition depth profile of thin-film materials, Curr. Opin. Colloid Interface Sci. **17**, 44 (2012).

[67] P. Balakrishnan, Universality of the role of hydrogen in superconductivity in nickelates, ISIS Neutron and Muon Source Data Journal (2024), https://doi.org/10.5286/ISIS.E.RB2320137.